J|A|C|S
ARTICLES
Published on Web 12/07/2005

Mechanism of N_2O Reduction by the μ_4-S Tetranuclear Cu_Z Cluster of Nitrous Oxide Reductase

Serge I. Gorelsky, Somdatta Ghosh, and Edward I. Solomon*

Contribution from the Department of Chemistry, Stanford University, Stanford, California 94305

Received September 1, 2005; E-mail: Edward.Solomon@stanford.edu

Abstract: Reaction thermodynamics and potential energy surfaces are calculated using density functional theory to investigate the mechanism of the reductive cleavage of the N−O bond by the μ_4-sulfide-bridged tetranuclear Cu_Z site of nitrous oxide reductase. The Cu_Z cluster provides an exogenous ligand-binding site, and, in its fully reduced $4Cu^I$ state, the cluster turns off binding of stronger donor ligands while enabling the formation of the Cu_Z-N_2O complex through enhanced $Cu_Z \rightarrow N_2O$ back-donation. The two copper atoms (Cu_I and Cu_{IV}) at the ligand-binding site of the cluster play a crucial role in the enzymatic function, as these atoms are directly involved in bridged N_2O binding, bending the ligand to a configuration that resembles the transition state (TS) and contributing the two electrons for N_2O reduction. The other atoms of the Cu_Z cluster are required for extensive back-bonding with minimal σ ligand-to-metal donation for the N_2O activation. The low reaction barrier (18 kcal mol^{-1}) of the direct cleavage of the N−O bond in the Cu_Z-N_2O complex is due to the stabilization of the TS by a strong $Cu_{IV}^{2+}-O^-$ bond. Due to the charge transfer from the Cu_Z cluster to the N_2O ligand, noncovalent interactions with the protein environment stabilize the polar TS and reduce the activation energy to an extent dependent on the strength of proton donor. After the N−O bond cleavage, the catalytic cycle consists of a sequence of alternating protonation/one-electron reduction steps which return the Cu_Z cluster to the fully reduced ($4Cu^I$) state for future turnover.

1. Introduction

During bacterial denitrification, an important process in environmental bioregulation and biodegradation,[1−4] N_2O is usually an intermediate of nitrite/nitrate denitrification and produced via reductive dimerization of NO in a reaction catalyzed by a membrane-bound NO reductase. In certain denitrifiers, N_2O respiration is lacking, leading to release of N_2O as the end product. In other organisms,[3,5] N_2O respiration can proceed independently from NO_2^-/NO_3^- respiration. In most denitrifying prokaryotes, denitrification provides a less energetically efficient alternative to aerobic respiration when the cell is under limiting supply of oxygen. As with oxygen respiration, this process is coupled to ATP synthesis.[6]

The denitrification pathway is an assembly of several, more or less independent processes, and all corresponding enzymes isolated to date have been identified as metalloproteins.[4] Nitrous oxide reduction requires a multi-copper enzyme, N_2O reductase (N_2OR). With respect to transition-metal content, two types of N_2ORs have been described in the literature: copper-only N_2ORs, which are head-to-tail homodimeric, soluble, periplasmic enzymes,[7−9] and copper−iron N_2ORs, which are homodimeric enzymes containing a *c*-type cytochrome as a component.[10−12] In the Cu-only N_2ORs, each subunit has two redox-active copper centers: a binuclear electron-transfer site Cu_A and a catalytic site termed Cu_Z. The neighboring Cu_A and Cu_Z centers belong to different subunits in the dimeric protein and are separated by ∼10 Å, while the intrasubunit distance between Cu_A and Cu_Z is ∼40 Å. The Cu_A center is thought to accept electrons from an electron donor (in vivo, the donors are a *c*-type cytochrome and/or pseudoazurin)[13−16] and transfer them to the neighboring Cu_Z site of another subunit of the N_2OR protein, where N_2O binds and is reduced to form N_2 and water.[8,17,18] In copper−iron N_2ORs, a *c*-type cytochrome center must transfer electrons to the neighboring Cu_Z site and, if a cytochrome *c* fragment is cleaved from the enzyme, the N_2O reduction activity is lost.[10]

(1) Payne, W. J. *Denitrification*; Wiley-Interscience: New York, 1981.
(2) Golterman, H. L., Ed. *Denitrification in the Nitrogen Cycle*; Plenum Press: New York, 1983.
(3) Zumft, W. G. In *The Prokaryotes: An Evolving Electronic Resource for the Microbiological Community*, 3rd ed., Release 3.19; Dworkin, M., Ed.; Springer-Verlag: New York, 2005.
(4) Eady, R. R.; Hasnain, S. S. In *Comprehensive Coordination Chemistry II*; McCleverty, J. A., Meyer, T. J., Eds.; Elsevier: Amsterdam, 2004; Vol. 8, p 759.
(5) Yoshinari, T. *Appl. Environ. Microbiol.* **1980**, *39*, 81.
(6) Zumft, W. G. *Microbiol. Mol. Biol. Rev.* **1997**, *61*, 533.
(7) Brown, K.; Djinovic-Carugo, K.; Haltia, T.; Cabrito, I.; Saraste, M.; Moura, J. J. G.; Moura, I.; Tegoni, M.; Cambillau, C. *J. Biol. Chem.* **2000**, *275*, 41133.
(8) Haltia, T.; Brown, K.; Tegoni, M.; Cambillau, C.; Saraste, M.; Mattila, K. *Biochem. J.* **2003**, *369*, 77.
(9) Brown, K.; Tegoni, M.; Prudencio, M.; Pereira, A. S.; Besson, S.; Moura, J. J. G.; Moura, I.; Cambillau, C. *Nature Struct. Biol.* **2000**, *7*, 191.
(10) Teraguchi, S.; Hollocher, T. C. *J. Biol. Chem.* **1989**, *264*, 1972−1979.
(11) Zhang, C. Q.; Jones, A. M.; Hollocher, T. C. *Biochem. Biophys. Res. Commun.* **1992**, *187*, 135.
(12) Mukonoweshuro, C.; Hollocher, T. C. *Arch. Biochem. Biophys.* **1993**, *306*, 195.
(13) Zhang, C. S.; Hollocher, T. C. *Biochim. Biophys. Acta* **1993**, *1142*, 253.
(14) Moir, J. W. B.; Ferguson, S. J. *Microbiology* **1994**, *140*, 389.
(15) Koutny, M.; Kucera, I.; Tesarik, R.; Turanek, J.; Van Spanning, R. J. M. *FEMS Lett.* **1999**, *488*, 157.
(16) Mattila, K.; Haltia, T. *Proteins: Struct., Funct., Bioinf.* **2005**, *59*, 708.
(17) Chen, P.; Cabrito, I.; Moura, J. J. G.; Moura, I.; Solomon, E. I. *J. Am. Chem. Soc.* **2002**, *124*, 10497.
(18) Chen, P.; Gorelsky, S. I.; Ghosh, S.; Solomon, E. I. *Angew. Chem., Intl. Ed.* **2004**, *43*, 4132.

 10.1021/ja055856o CCC: $33.50

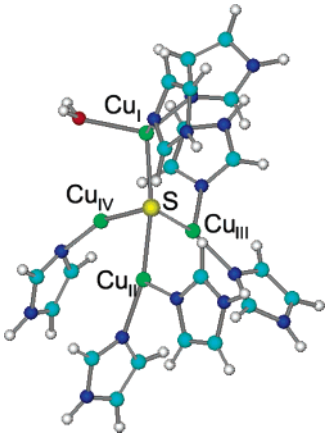

Figure 1. Structure of the Cu_Z site of N_2OR. The H_2O ligand is shown at the Cu_I/Cu_{IV} edge of the cluster.

Cu_Z is a novel μ_4-sulfide-bridged tetranuclear Cu cluster with a distorted tetrahedral shape (Figure 1). Three of the copper atoms, Cu_I, Cu_{II}, and Cu_{III}, are coordinated by two histidine ligands, whereas Cu_{IV} has only one histidine ligand. There is also an exogenous ligand-binding site at the Cu_I/Cu_{IV} edge of the cluster. The resting form of N_2OR has been characterized spectroscopically and shown to contain the Cu_Z cluster in the $1Cu^{II}/3Cu^{I}$ redox state with a total spin of $^1/_2$.[17,19−21] According to the EPR data and DFT calculations, the spin density is delocalized between two or more Cu ions and the μ_4-sulfide, indicating that the cluster is a mixed-valence system.[17−20]

Recently, we have determined that the catalytically active form of the Cu_Z cluster is the fully reduced $4Cu^{I}$ form.[22] This finding has been confirmed by Dooley and co-workers.[23] We also proposed that the competitive N_2O binding to Cu_Z is better in the $4Cu^{I}$ redox form than in the resting $1Cu^{II}/3Cu^{I}$ redox form due to enhanced back-donation from the $Cu_Z(4Cu^{I})$ cluster to the μ-1,3-bridged N_2O ligand.[18]

Previously reported reactions of N_2O in homogeneous systems involved complexes of transition metals (Ti,[24,25] V,[26,27] Cr,[27,28] Fe,[29,30] Co,[31−36] Ni,[37,38] Zr,[39] Mo,[40] Ru,[41−48] Rh,[31] and Hf [49]) in low oxidation states. Since N_2O is a weak ligand with a low binding energy and the N_2O complex formed with a redox-active metal (such as Ti^{II} and V^{II}) can be rapidly converted to N_2 and metal-oxidized species, $O{=}M^{n+2}$, N_2O complexes are usually detected only as transient species, and no X-ray structures are available in the literature.

In the most characterized metal−N_2O complex, $[Ru^{II}(NH_3)_5(N_2O)]^{2+}$, the N_2O ligand has been found to coordinate to the Ru^{II} ion in a linear end-on mode through the terminal N atom, and the stability constants of the complexes and related thermochemical parameters have been obtained.[41,42,45,46,48] Metal−N_2O bonding in this complex has been examined.[48,50] It was also determined that N_2O is a weaker ligand for Ru^{II} than dinitrogen.[41]

Among the known reactions of N_2O are its oxygen atom transfer to transition-metal complexes,[24−28,51]

$$N_2O + M^{n+} \rightarrow O{=}M^{n+2} + N_2 \qquad (1)$$

and to phosphine, hydride, aryl, and alkyl ligands in the Co, Ni, Zr, and Hf complexes:[38,39,49]

$$N_2O + L{-}M^{n+} \rightarrow L{-}O{-}M^{n+} + N_2 \qquad (2)$$

In the synthesis of oxo-bridged Ti, V, and Cr clusters, N_2O acts as a source of the bridging oxygen atoms.[27] $M_a{-}N{-}N{-}O{-}M_b$ bridged species have been proposed as possible intermediates in the reductive cleavage of the N−O bond in the Ru^{II} and Co^{I} complexes.[33,43,47] The significance of the bridged species with respect to its role in activation of N_2O has not been discussed in the literature.

In this paper, we investigate the mechanism of the N_2O reduction by the μ_4-sulfide-bridged tetranuclear Cu_Z site of N_2-OR using density functional calculations. We evaluate the reductive cleavage of the N−O bond at the Cu_Z site, the geometric and electronic structure changes in the subsequent steps of the catalytic cycle, the role of the μ_4-sulfide-bridged tetranuclear copper site in the catalysis, and, in particular, the involvement of back-bonding in the binding and activation of N_2O.

2. Computational Details

Density functional theory (DFT) calculations have been performed using the Gaussian 03 program.[52] Optimized molecular geometries were calculated using the BP86 and B3LYP exchange-correlation functionals[53−55] and using the GDIIS[56,57] algorithm. The spin-unrestricted

(19) Chen, P.; George, S. D.; Cabrito, I.; Antholine, W. E.; Moura, J. J. G.; Moura, I.; Hedman, B.; Hodgson, K. O.; Solomon, E. I. *J. Am. Chem. Soc.* **2002**, *124*, 744.
(20) Oganesyan, V. S.; Rasmussen, T.; Fairhurst, S.; Thomson, A. J. *Dalton Trans.* **2004**, 996.
(21) Rasmussen, T.; Berks, B. C.; Butt, J. N.; Thomson, A. J. *Biochem. J.* **2002**, 807.
(22) Ghosh, S.; Gorelsky, S. I.; Chen, P.; Cabrito, I.; Moura, J. J. G.; Moura, I.; Solomon, E. I. *J. Am. Chem. Soc.* **2003**, *125*, 15708.
(23) Chan, J. M.; Bollinger, J. A.; Grewell, C. L.; Dooley, D. M. *J. Am. Chem. Soc.* **2004**, *126*, 3030.
(24) Bottomley, F.; Brintzinger, H. H. *J. Chem. Soc., Chem. Commun.* **1978**, 234.
(25) Bottomley, F.; Lin, I. J. B.; Mukaida, M. *J. Am. Chem. Soc.* **1980**, *102*, 5238.
(26) Bottomley, F.; White, P. S. *J. Chem. Soc., Chem. Commun.* **1981**, 28.
(27) Bottomley, F.; Paez, D. E.; White, P. S. *J. Am. Chem. Soc.* **1982**, *104*, 5651.
(28) Bottomley, F.; Paez, D. E.; White, P. S. *J. Am. Chem. Soc.* **1981**, *103*, 5581.
(29) Bayachou, M.; Elkbir, L.; Farmer, P. J. *Inorg. Chem.* **2000**, *39*, 289.
(30) Immoos, C. E.; Chou, J.; Bayachou, M.; Blair, E.; Greaves, J.; Farmer, P. J. *J. Am. Chem. Soc.* **2004**, *126*, 4934.
(31) Banks, R. G. S.; Henderson, R. J.; Pratt, J. M. *Chem. Commun.* **1967**, 387.
(32) Yamamoto, A.; Kitazume, S.; Pu, L. S.; Ikeda, S. *J. Am. Chem. Soc.* **1971**, *93*, 371.
(33) Collman, J. P.; Marrocco, M.; Elliott, M. C.; L'Her, M. *J. Electroanal. Chem.* **1981**, *124*, 113.
(34) Jhang, J.; Tse, Y.-H.; Lever, A. B. P.; Pietro, W. J. *J. Porphyrins Phthalocyanines* **1997**, *1*, 323.
(35) Drummond, J. T.; Matthews, R. G. *Biochemistry* **1994**, *33*, 3732.
(36) Drummond, J. T.; Matthews, R. G. *Biochemistry* **1994**, *33*, 3742.
(37) Taniguchi, I.; Shimpuku, T.; Yamashita, K.; Ohtaki, H. *J. Chem. Soc., Chem. Commun.* **1990**, 915.
(38) Matsunaga, P. T.; Hillhouse, G. L. *J. Am. Chem. Soc.* **1993**, *115*, 2075.
(39) Vaughan, G. A.; Hillhouse, G. L.; Lum, R. T.; Buchwald, S. L.; Rheingold, A. L. *J. Am. Chem. Soc.* **1988**, *110*, 7215.
(40) Cooper, N. J.; Green, M. L. H.; Couldwell, C.; Prout, K. *J. Chem. Soc., Chem. Commun.* **1977**, 145.
(41) Armor, J. N.; Taube, H. *J. Am. Chem. Soc.* **1969**, *91*, 6874.
(42) Armor, J. N.; Taube, H. *J. Am. Chem. Soc.* **1970**, *92*, 2560.
(43) Armor, J. N.; Taube, H. *Chem. Commun.* **1971**, 287.
(44) Armor, J. N.; Taube, H. *J. Am. Chem. Soc.* **1971**, *93*, 6476.
(45) Bottomley, F.; Crawford, J. R. *J. Am. Chem. Soc.* **1972**, *94*, 9092.
(46) Bottomley, F.; Brooks, W. V. F. *Inorg. Chem.* **1977**, *16*, 6.
(47) Groves, J. T.; Roman, J. S. *J. Am. Chem. Soc.* **1995**, *117*, 5594.
(48) Paulat, F.; Kuschel, T.; Nather, C.; Praneeth, V. K. K.; Sander, O.; Lehnert, N. *Inorg. Chem.* **2004**, *43*, 6979.
(49) Vaughan, G. A.; Rupert, P. B.; Hillhouse, G. L. *J. Am. Chem. Soc.* **1987**, *109*, 5538.
(50) Tuan, D. F.-T.; Hoffmann, R. *Inorg. Chem.* **1985**, *24*, 871.
(51) Bottomley, F.; Lin, I. J. B.; White, P. S. *J. Am. Chem. Soc.* **1981**, *103*, 703.
(52) Frisch, M. J.; et al. *Gaussian 03*, Revision C.01.

DFT method was employed to model the open-shell species, and the broken-symmetry (BS) approach[58] was used to obtain open-shell singlet-spin states. Because the BS singlet state does not correspond to a pure singlet state, an approximate spin projection method[58] was used to derive the corrected energy of the singlet state (E_S):

$$E_S = E_T - 2(E_T - E_{BS})$$

where E_{BS} and E_T are the energies of the BS solution of the singlet state and the triplet state, respectively.

Zero-point vibrational energies (ZPE) and thermal corrections (0 → 298 K) were added on the basis of B3LYP frequency calculations (unscaled) using the same basis set as for the geometry optimizations.

The Cu_Z active site has been modeled as a μ_4-sulfide-bridged tetranuclear active site with seven histidine amino acid residues as imidazoles. The mixed triple-ζ/double-ζ (6-311++G** on the active center (Cu_4SN_7L) and 6-31G* on the other atoms) basis set and tight self-consistent field convergence criteria were used for calculations. Calculations of the $[Ru(NH_3)_5(N_2O)]^{2+}$ complex were done using the DZVP basis set[59] for Ru and the TZVP basis set[60] for the other atoms. The polarized continuum model (PCM)[61] with a dielectric constant of $\epsilon = 4$ was employed to simulate the protein environment around the catalytic site. A probe radius of 1.40 Å, corresponding to the water molecule, was chosen. The calculated solvation energies (using the united atom topological model with the default UAHF settings) of the $[Cu_4S(im)_7L]^{q+}$ complexes are between −66 and −71 kcal mol^{-1} for the $q = +2$ species and between −165 and −167 kcal mol^{-1} for the $q = +3$ species, and they depend weakly on the Cu_I/Cu_{IV} edge ligand L. The above solvation energy values are in close agreement to those calculated using the Born equation. If not specified otherwise, the calculated results are reported at the B3LYP level using the PCM model with $\epsilon = 4$ and the mixed basis set specified above. The results of the BP86 calculations were fairly similar to those obtained using the B3LYP functional (Table S1, Supporting Information) but gave a more covalent description of the metal−ligand bonds. The gas-phase geometries were used for the analysis. The PCM geometry optimizations were conducted for several Cu_Z complexes. As was demonstrated for other systems,[62] the change of geometry by the solvation effects was not very large, and the differences in electronic energies between the PCM optimized structures and the single-point PCM calculations using the gas-phase geometries were usually less than 2 kcal mol^{-1}.

Wave function stability calculations were performed to confirm that the calculated wave functions corresponded to the ground state. The counterpoise corrections have been applied to calculated binding energies in order to account for basis set superposition errors (BSSE).[63]

The X-ray structures of *Pseudomonas denitrificans* N_2OR (PDB code 1FWX)[7,8] and *Pseudomonas nautica* N_2OR (PDB code 1QNI)[7,9] indicate that the orientations of the imidazole side chains of the histidine ligands around the Cu_4S cluster are determined by covalent links with the protein backbone and a network of hydrogen bonds (through the N−H bonds of the imidazole rings). To evaluate Cu_Z models with these structural constraints, two types of partial geometry optimizations were performed. In the first model, the positions of carbon atoms that correspond to the C_γ atoms of the histidine ligands (i.e., C6, C11, C16, C21, C26, C31, and C36; see Figure S1 for atom numbering) were frozen to those derived from the 1.6-Å-resolution X-ray structure of *P. denitrificans* N_2OR. In the second model, in addition to fixing the C_γ positions, the positions of the remote N atoms of the imidazoles, all involved in H-bonds (i.e. N10, N12, N17, N22, N27, N32, and N40; see Figure S1), were frozen. The significance of these constraints is discussed in section 3.5.3.

The proton solvation energy in water was taken as −262.23 kcal mol^{-1} from high-quality calculations of the water clusters.[64] This value results in the absolute potential for the standard hydrogen electrode (SHE) of −4.50 V, in close agreement with the experimental estimate, −4.43 V.[65] The −4.50 V value for the absolute potential of the SHE was used in this work to calculate electron-transfer driving forces. Protonation and reduction free energies were calculated using the scheme described in ref 66. All calculated thermochemical parameters refer to 298.15 K. The electron-transfer driving forces between the Cu_Z and Cu_A centers were calculated using the redox potential of the Cu_A center in N_2OR, +0.26 V vs SHE.[21] This value is in close agreement with the redox potential of the Cu_A center in other proteins[67,68] and the calculated redox potential of the Cu_A model.[69]

For the N_2O potential energy surface (PES) calculations in the gas phase, the 6-311+G(3df) basis set was used for all atoms. For perturbed Cu_Z cluster models (sections 3.3−3.4), the BP86/LanL2DZ calculations were employed to enable reaction coordinate calculations on a reasonable time scale. Frequency calculations at the BP86/LanL2DZ level of theory were used to derive the ZPE and thermal corrections for $\Delta G^{\ddagger}$. According to these calculations, the ZPE and entropy corrections change the activation energy of the N−O bond cleavage by −1.3 and +2.1 kcal mol^{-1}, respectively.

Molecular orbital (MO) compositions, the overlap populations between molecular fragments, and bond orders were calculated using the AOMix program.[70,71] Single-point PCM($\epsilon = 4$) calculations with the TZVP basis set[60] for all atoms were used for molecular orbital analysis. Atomic charges and spin densities were calculated using Mulliken[72] and natural[73] population analysis (MPA and NPA, respectively) as implemented in Gaussian 03. The Mayer bond orders[74,75] were obtained to analyze the chemical bonding between the molecular fragments. The bond order contributions from α- and β-spin molecular orbitals were calculated (BO^{α} and BO^{β}, respectively) and used in the analysis of chemical bonding.[74] The analysis of the MO compositions in terms of fragment molecular orbitals (FOs) was performed using AOMix-CDA.[70,74]

2.1. Charge Decomposition. The charge decomposition analysis (CDA)[76] was performed to quantify the charge donation and back-donation between the metal fragment and the N_2O ligand in the $[Cu_4S(im)_7(N_2O)]^{2+}$ and $[Ru(NH_3)_5(N_2O)]^{2+}$ complexes (Table S2). However, the difference between N_2O-to-metal donation and metal-to-N_2O back-donation in Table S2 was not equal to the net charge transfer from the metal fragment to the N_2O ligand. This is related to the fact that, in CDA,[76] the terms *donation* and *back-donation* correspond to an overall reorganization of electronic density, which includes the intrafragment reorganization as well as charge transfer (CT).

(53) Perdew, J. P. *Phys. Rev. B* **1986**, *33*, 8822.
(54) Becke, A. D. *Phys. Rev. A* **1988**, *38*, 3098.
(55) Becke, A. D. *J. Chem. Phys.* **1993**, *98*, 5648.
(56) Farkas, O.; Schlegel, H. B. *J. Chem. Phys.* **1998**, *109*, 7100.
(57) Farkas, O.; Schlegel, H. B. *J. Chem. Phys.* **1999**, *111*, 10806.
(58) Li, J.; Noodleman, L.; Case, D. A. In *Inorganic Electronic Structure and Spectroscopy*; Solomon, E. I., Lever, A. B. P., Eds.; John Wiley & Sons: New York, 1999; Vol. 1, p 661.
(59) Godbout, N.; Salahub, D. R.; Andzelm, J.; Wimmer, E. *Can. J. Chem.* **1992**, *70*, 560.
(60) Schafer, A.; Huber, C.; Ahlrichs, R. *J. Chem. Phys.* **1994**, *100*, 5829.
(61) Barone, V.; Cossi, M.; Tomasi, J. *J. Comput. Chem.* **1998**, *19*, 404.
(62) Baik, M. H.; Friesner, R. A. *J. Phys. Chem. A* **2002**, *106*, 7407.
(63) Boys, S. F.; Bernardi, F. *Mol. Phys.* **1970**, *19*, 553.
(64) Tawa, G. J.; Topol, I. A.; Burt, S. K.; Caldwell, R. A.; Rashin, A. A. *J. Chem. Phys.* **1998**, *109*, 4852.
(65) Reiss, H.; Heller, A. *J. Phys. Chem.* **1985**, *89*, 4207.
(66) Ullmann, G. M.; Noodleman, L.; Case, D. A. *J. Biol. Inorg. Chem.* **2002**, *7*, 632.
(67) Hwang, H. J.; Lu, Y. *Proc. Natl. Acad. Sci. U.S.A.* **2004**, *101*, 12842.
(68) Hwang, H. J.; Berry, S. M.; Nilges, M. J.; Lu, Y. *J. Am. Chem. Soc.* **2005**, *127*, 7274.
(69) Gorelsky, S. I.; Solomon, E. I., unpublished results.
(70) Gorelsky, S. I., *AOMix: Program for Molecular Orbital Analysis*; York University: Toronto, Canada (http://www.sg-chem.net).
(71) Gorelsky, S. I.; Lever, A. B. P. *J. Organomet. Chem.* **2001**, *635*, 187.
(72) Mulliken, R. S. *J. Chem. Phys.* **1955**, *23*, 1833.
(73) Reed, A. E.; Weinstock, R. B.; Weinhold, F. *J. Chem. Phys.* **1985**, *83*, 735.
(74) Gorelsky, S. I.; Basumallick, L.; Vura-Weis, J.; Sarangi, R.; Hedman, B.; Hodgson, K. O.; Fujisawa, K.; Solomon, E. I. *Inorg. Chem.* **2005**, *44*, 4947.
(75) Mayer, I. *Chem. Phys. Lett.* **1983**, *97*, 270.
(76) Dapprich, S.; Frenking, G. *J. Phys. Chem.* **1995**, *99*, 9352.

Scheme 1. Composition of Occupied and Unoccupied Molecular Orbitals of the Complex AB in Terms of Occupied (OFOs) and Unoccupied (UFOs) Molecular Orbitals of Fragments A and B[a]

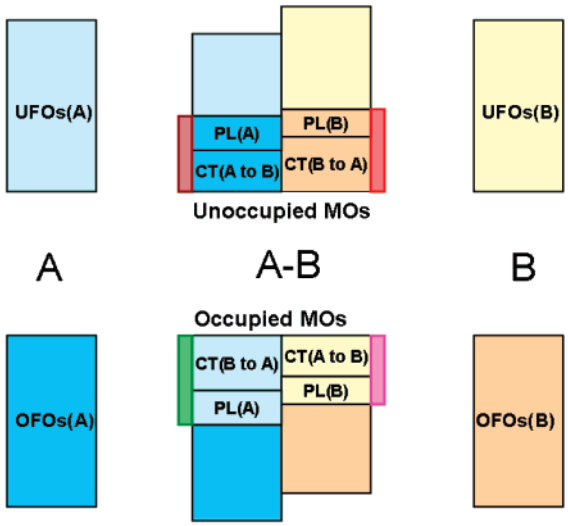

PL(A) + CT(A to B) = %OFO(A) in unoccupied MOs (A-B) (1)
PL(A) + CT(B to A) = %UFO(A) in occupied MOs (A-B) (2)
PL(B) + CT(B to A) = %OFO(B) in unoccupied MOs (A-B) (3)
PL(B) + CT(A to B) = %UFO(B) in occupied MOs (A-B) (4)

[a] Contributions from charge-transfer (CT) and polarization (PL) interactions are shown. The fragment orbital contributions and (1)−(4) are color-coded to help the reader.

When fragments A and B are combined to form a bond, there are two types of electronic interactions that will affect the compositions of the resulting MOs of the A−B complex. These are CT from donor to acceptor and electronic polarization (PL) of one fragment in the presence of another. The CT interaction mixes the occupied fragment molecular orbital (OFO) of the donor with the unoccupied fragment molecular orbital (UFO) of the acceptor and, thus, transfers the electron density from donor to acceptor. The electronic polarization of one molecular fragment in the presence of the other fragments induces mixing between its OFOs and UFOs and does not shift electron density from one fragment to another. Instead, it adjusts the electronic distribution within this fragment. Thus, in calculation of donation and back-donation between molecular fragments, one should treat CT and PL terms separately, including only the CT terms in the decomposition.

The MO coefficient matrix in the basis of atomic orbitals can be transformed to the MO coefficient matrix in the FO basis. This is done in the following four steps:

1. Calculate the MOs of the complex.

2. Calculate the MOs of all fragments and combine the resulting linear combination of atomic orbitals (LCAO-MO) matrices into one to form the FO basis set.

3. Calculate the eigenvectors of the complex in the FO basis.

4. Transform the AO overlap matrix to the FO overlap matrix, and calculate the FO populations (MPA) and their contributions to occupied and unoccupied MOs of the complex.

In this linear combination of fragment molecular orbitals (LCFO-MO) approach, the orbital interactions between molecular fragments can be separated into CT and PL terms (Scheme 1). For example, the net PL contribution, PL(A) − PL(B), can be calculated by subtracting (3) from (2) (Scheme 1), and the net CT from fragment A to fragment B, CT(A to B) − CT(B to A), can be calculated by subtracting (2) from (1).

Thus, the extended CDA (ECDA) method, based on Scheme 1, was used to estimate both CT and PL contributions to N_2O binding in the Cu_Z cluster and in the $[Ru(NH_3)_5(N_2O)]^{2+}$ complex used as a reference (Table S3). A more detailed description of ECDA will be provided elsewhere.[69,70]

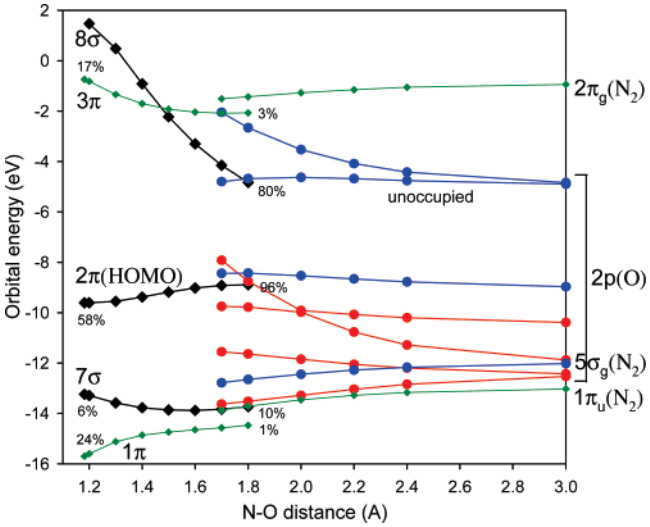

Figure 2. Frontier molecular orbitals of N_2O as a function of the N−O distance (the linear nuclear configuration). The N_2O geometries correspond to those in Figure 2. Black lines correspond to σ orbitals of the singlet state; red and blue lines indicate the α- and β-spin σ orbitals of 2p(O) and $5\sigma_g(N_2)$ character of the triplet state, respectively; green lines correspond to π_u and π_g orbitals of N_2. The percentages indicate the O atom character in the corresponding molecular orbitals of N_2O in the singlet state.

2.2. Analysis of Binding Energies. The binding energies, E_o, between the metal site and the N_2O ligand are partitioned into two contributions, E_{prep} and E_{int}:[74]

$$E_o = E_{int} + E_{prep}$$

E_{int} is the interaction energy between the Cu_Z site and the N_2O ligand in the complex. E_{prep} is the deformation energy necessary to deform the Cu_Z site and the N_2O ligand from their equilibrium geometries to the geometry they acquire in the Cu_Z-N_2O complex:

$$E_{prep} = E_{prep}(Cu_Z) + E_{prep}(N_2O)$$

3. Results and Analysis

3.1. Reaction Mechanism of N_2O Dissociation in the Gas Phase. Nitrous oxide is known to have a linear structure in its global energy minimum.[77−80] The N−N bond distance is 1.128 (expt) or 1.121 Å (B3LYP/6-311+G(3df)), which is between the distances expected for a N−N triple bond (1.098 Å) and a double bond (1.25 Å). The N−O bond distance is 1.184 (expt) or 1.182 Å (B3LYP), which is intermediate between the distances expected for a double bond (1.15 Å) and a single bond (∼1.4 Å). This may be explained in terms of the resonance between the structures $N{\equiv}N^+{-}O^-$ and $N^-{=}N^+{=}O$. These resonance structures also explain the calculated charge distribution in N_2O (NPA charges: $N_t^{-0.08}{-}N_c^{+0.40}{-}O^{-0.32}$). The electron configuration of near-equilibrium N_2O ($X\ ^1\Sigma^+$) is $1\sigma^2...6\sigma^2 1\pi^4 7\sigma^2 2\pi^4$ (Figure 2, $d_{N-O} = 1.182$ Å), with the lowest-lying triplet states corresponding to the $2\pi \rightarrow 3\pi$ electron excitation. The 1π molecular orbital is bonding, 2π (with the composition of 38% N_t, 4% N_c, 58% O orbital character) is weakly antibonding, and 3π (47% N_t, 36% N_c, 17% O) is

(77) Chang, A. H. H.; Yarkony, D. R. *J. Chem. Phys.* **1993**, *99*, 6824.
(78) Tachikawa, H.; Hamabayashi, T.; Yoshida, H. *J. Phys. Chem.* **1995**, *99*, 16630.
(79) Nakamura, H.; Kato, S. *J. Chem. Phys.* **1999**, *110*, 9937.
(80) Hwang, D.-Y.; Mebel, A. M. *Chem. Phys.* **2000**, *259*, 89.

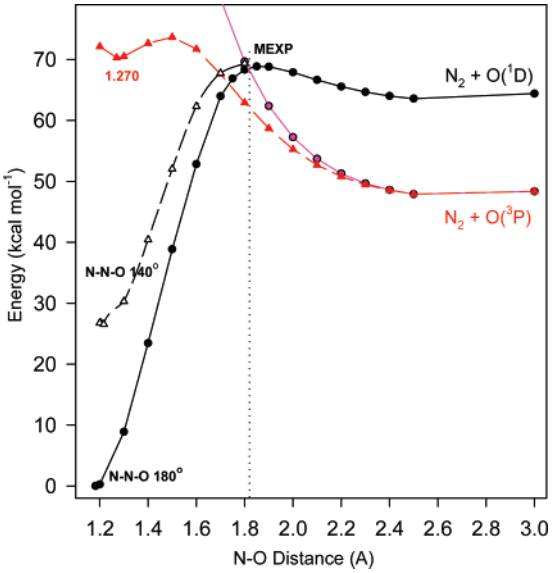

Figure 3. Potential energy surfaces for lowest-energy singlet (black lines) and triplet (red lines) states of N_2O as derived from spin-unrestricted B3LYP/6-311+G(3df) calculations. Solid lines correspond to the linear N_2O geometry, dashed lines correspond to the bent N_2O geometry ($\angle N-N-O \approx 122°$ for the triplet), and MEXP is the minimum energy crossing point.

strongly antibonding with respect to the N−O bond. As a result, N_2O with a linear geometry has a triplet excited-state surface resulting from the $1\sigma^2...6\sigma^2 1\pi^4 7\sigma^2 2\pi^3 3\pi$ electron configuration which is repulsive with respect to the N−O bond (no local minimum at a short N−O distance, Figure 3). Upon elongation of the N−O bond, the HOMO (2π) becomes increasingly localized on the O atom. In parallel, the antibonding 8σ orbital gains O character, and its energy decreases because of the loss in its N−O antibonding character (Figure 2).

At $d_{N-O} \approx 1.8$ Å (Figure 3, red circles), the singlet−triplet spin crossover becomes an energetically favorable process and allows N_2O dissociation, with the N_2 molecule and the $O(^3P)$ atom as products:

$$N_2O(^1\Sigma^+) \rightarrow N_2(^1\Sigma^+_g) + O(^3P) \qquad (3)$$

In this spin-forbidden dissociation of N_2O, the lowest-energy fragmentation of N_2O into N_2 and $O(^3P)$ is endothermic (expt 38.5 kcal mol^{-1}).[81,82] According to the multireference configuration interaction (MRCI) calculations,[77,80] the minimum energy crossing point (MEXP) on the singlet−triplet intersection corresponds to a linear geometry with a N−O distance of ∼1.8 Å. The computed activation energy for N_2O decomposition (60.3 kcal mol^{-1}) at the MRCI level of theory[80] is in good agreement with the experimentally[81] observed value (∼59 kcal mol^{-1}). The B3LYP calculations predict a higher activation energy, 71.4 kcal mol^{-1} (Figure 3).

The singlet−triplet crossing can also occur at the bent N−N−O geometry. The energy of the corresponding MEXP is 77.5 (MRCI)[80] or 70.1 kcal mol^{-1} (B3LYP, Figure 3). DFT calculations predict almost equal activation energy for the N−O bond cleavage for the bent and linear N−N−O geometries. According to the B3LYP calculations, the triplet potential energy surface with the bent configuration does have a local energy minimum at $d_{N-O} = 1.27$ Å and N−N−O angle of 122.5° (Figure 3, red triangles). For the linear nuclear configuration, the corresponding triplet surface is only repulsive with respect to the N−O interaction. The bent N−N−O geometry is relevant for the N−O bond cleavage at the catalytic site of N_2OR (vide infra).

Scheme 2. Possible Steps of Two-Electron, Two-Proton Reduction of N_2O at the Catalytic Site of N_2OR

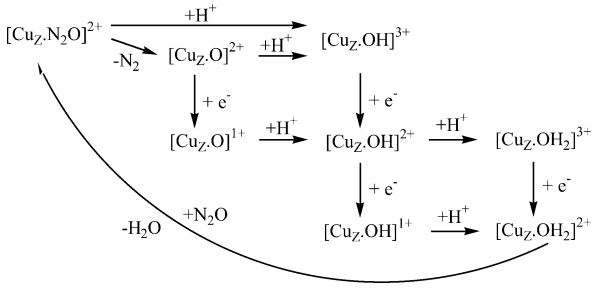

3.2. Reaction Mechanism of N_2O Dissociation at the Catalytic Site of N_2OR. The catalytically active form of Cu_Z is an electron-rich site with four Cu^I atoms. The most probable catalytic cycle, which involves the two-electron, two-proton reduction of N_2O, can be considered using Scheme 2. From this scheme, it can be seen that certain steps in the catalytic cycle (including intermolecular electron transfer between the electron donor, such as cytochrome c[13] or methyl viologen,[22] and N_2OR) may display (depending on their thermodynamic and kinetic parameters) a pH dependence, and the relative rates of protonation of the $[Cu_Z{\cdot}OH_x]$ species and electron transfer to Cu_Z will influence which reaction intermediates can be trapped and observed experimentally. In addition, the N−O cleavage step can be coupled with a protonation of the $[Cu_Z{\cdot}O]^{2+}$ species (Scheme 2). Kinetic studies of N_2ORs do indicate that there is a pH dependence of enzyme activity.[83,84] The N_2OR activity increases as the pH increases, reaches a maximum at pH 8−9, and then decreases.

As we previously determined,[18,22] N_2O binds at the substrate-binding Cu_I/Cu_{IV} edge. The N_2O ligand can bind in several coordination modes, of which the most stable are a linear end-on mode with the terminal nitrogen atom coordinating to Cu_I and a bent μ-1,3 bridging mode with the terminal nitrogen atom coordinating to Cu_I and the oxygen atom coordinating to Cu_{IV} (Figure 4, reactant complexes).

The calculated energy of gas-phase binding of N_2O to the Cu_Z ($4Cu_I$) cluster is −5.3 (Figure 4) or −2.3 kcal mol^{-1} (B3LYP calculations, Table S1), and the end-on mode is more favorable than the μ-1,3 bridging mode (by 1.2 kcal mol^{-1}, Figure 4). However, in the dielectric continuum calculations at the PCM($\epsilon = 4$) level, the μ-1,3 bridging mode is more favorable than the end-on mode (Table S1). The μ-1,3 bridging mode becomes more stable in the dielectric environment than the linear end-on mode because it features much greater charge transfer from the Cu_Z cluster to the N_2O ligand ($q(N_2O) = -0.49$ vs −0.12 au, Figure 4), and, as a result, the energy of $[Cu_4S(im)_7(\mu\text{-}1,3\text{-}N_2O)]^{2+}$ becomes lower than the energy of the Cu_Z-N_2O complex with a linear N-end-on coordination of N_2O (by 3.1 kcal mol^{-1}). In N_2OR, hydrogen-bonding interactions of the

(81) Johnston, H. S. *J. Chem. Phys.* **1951**, *19*, 663.
(82) Jolly, W. L. *The Inorganic Chemistry of Nitrogen*; W. A. Benjamin, Inc.: Amsterdam, 1964.
(83) Yamaguchi, K.; Kawamura, A.; Ogawa, H.; Suzuki, S. *J. Biochem.* **2003**, *134*, 853.
(84) Ghosh, S.; Gorelsky, S. I.; Solomon, E. I., unpublished results.

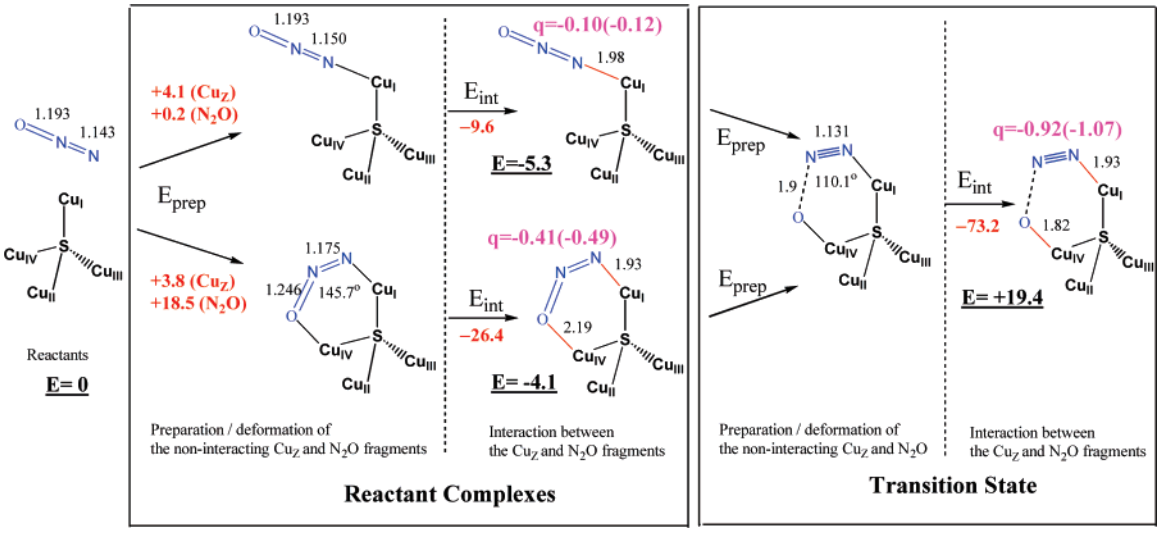

Figure 4. Deformation energies (E_{prep}) of the Cu_Z and N_2O fragments, electronic interaction energies (E_{int}) between Cu_Z and N_2O, the net relative energies (E) for the reactant complexes and the transition state, and the total NPA charge (q) of the N_2O ligand in the species (BP86 calculations). Bond lengths and electronic energies are given in Å and kcal mol^{-1}, respectively; $q(N_2O)$ from BP86/PCM($\epsilon = 4$) calculations is shown in parentheses.

nitrous oxide O atom with the side chain of a neighboring conserved lysine residue[8] can also help to stabilize the complex with the μ-1,3 binding mode. Other modes of binding of N_2O to the Cu_Z cluster are ~3−5 kcal mol^{-1} higher in energy.

The weak binding energy to a metal site is a signature of the N_2O ligand,[41] which is known to be a weak σ donor and a weak π acceptor.[50] The N−N and N−O bond distances of the N_2O ligand in the $[Cu_4S(im)_7(\mu\text{-}1,3\text{-}N_2O)]^{2+}$ complex are 0.03 and 0.05 Å longer, respectively, than those in a free N_2O molecule (Figure 4, reactant complexes). The bending of the N_2O fragment ($\angle$N−N−O = 145.7° (gas-phase), 139.6° (PCM(ϵ = 4) optimization))[85] from the linear geometry raises its electronic energy by 18.0 kcal mol^{-1}. The N−N and N−O bond deformations are small and contribute only 0.5 kcal mol^{-1} to the deformation energy of the N_2O fragment ($E_{prep}(N_2O)$ = 18.5 kcal mol^{-1}, Figure 4) in the $[Cu_4S(im)_7(\mu\text{-}1.3\text{-}N_2O)]^{2+}$ complex. The bending of the N_2O ligand results in a 2 eV splitting of the doubly degenerate LUMO (3π orbital, Figure 2) of N_2O into two lower-energy, nondegenerate π^* orbitals.[22] The low-energy LUMO of the bent N_2O ligand can now strongly couple with the occupied Cu_I/Cu_{IV}-localized d orbitals, forming a back-bond between the N_2O ligand and the Cu_Z cluster and transferring charge from Cu_I and Cu_{IV} to the N_2O ligand The LUMO of the $[Cu_4S(im)_7(\mu\text{-}1.3\text{-}N_2O)]^{2+}$ complex has 61% π^* LUMO(N_2O) character, with 3d orbital contributions of 14% from Cu_I and 8% from Cu_{IV}. This very significant back-bonding interaction is further confirmed by the NPA, which indicates a large negative charge of the N_2O ligand in the μ-1,3 complex (Figure 4). As a result of this significant back-bonding, the stronger Cu_I−N and Cu_{IV}−O interactions and weaker N−N and N−O bonds (E_{int} = −26.4 kcal mol^{-1}, Figure 4) compensate the large deformation energy of the N_2O ligand (+18.5 kcal mol^{-1}, Figure 4), and the resulting $[Cu_4S(im)_7(\mu\text{-}1.3\text{-}N_2O)]^{2+}$ complex is more stable in the dielectric medium than the complex with the end-on coordination mode of N_2O (Table S1). Moreover, the N_2O structure in the former is "molded" to a geometry that resembles the transition state (TS), activating the N_2O ligand for both direct and proton-assisted (section 3.3) N−O bond cleavage.

In contrast, the $[Cu_4S(im)_7N_2O]^{2+}$ complex with linear coordination of N_2O to the Cu_4S cluster exhibits much less charge transfer from the Cu_Z cluster to the N_2O ligand ($q(N_2O)$ = −0.1 au, Figure 4), and the N−N and N−O bonds of the N_2O ligand remain relatively unperturbed relative to those in the gas-phase N_2O molecule. Moreover, the charge of the oxygen atom (q_{NPA} = −0.26 au) of the N_2O ligand is less negative than its free ligand value (−0.32 au). Thus, the N_2O ligand in the Cu_Z−N_2O complex with an end-on coordination mode is not activated for direct or proton-assisted N−O bond cleavage.

Cleavage of the N−O bond in the $[Cu_4S(im)_7N_2O]^{2+}$ complex,

$$[Cu_4S(im)_7N_2O]^{2+} \rightarrow N_2 + [Cu_4S(im)_7O]^{2+} \qquad (4)$$

is exothermic (ΔG_r = −28.8 kcal mol^{-1} at the B3LYP/PCM(ϵ = 4) level) and may go through the intersection of the singlet and triplet surfaces (Figure 5A) or may occur entirely on a spin-singlet surface. In both cases, the computed activation energy is ~24 kcal mol^{-1} (gas-phase), and the TS (or MEXP in case of the singlet−triplet crossing) corresponds to a N−O internuclear distance of ~1.9−2.0 Å, which is ~0.1−0.2 Å longer than that for the gas-phase N_2O dissociation. The existence of the spin-singlet TS can be confirmed by a frequency calculation which has one imaginary frequency mode (corresponding to N−O bond stretching). The ZPE and entropy corrections (section 2) are small and cancel each other, resulting in a 1 kcal mol^{-1} difference between calculated $\Delta G^{\ddagger}$ and $\Delta E^{\ddagger}$. The bond order analysis (Figure 5B) indicates that the breaking of the N−O bond of nitrous oxide is synchronized with the strengthening of the N−N and Cu_{IV}−O bonds, obeying the bond order conservation rule.[86,87]

In the initial stage of the reaction coordinate (where the N−O distance is elongated up to 1.85 Å), the charge transfer from the Cu_4S cluster to the N_2O fragment increases to −1.07 au, with much of the electron density coming from Cu_{IV} (Figure 5C). The N−N and Cu_{IV}−O bonds gain strength (the corre-

(85) The previously published geometry[22] with a N−N−O angle of 139° was obtained at the BP86/LanL2DZ level of optimization.

(86) Johnston, H. S. *Adv. Chem. Phys.* **1960**, *85*, 131.
(87) Johnston, H. S.; Parr, C. *J. Am. Chem. Soc.* **1963**, *85*, 2544.

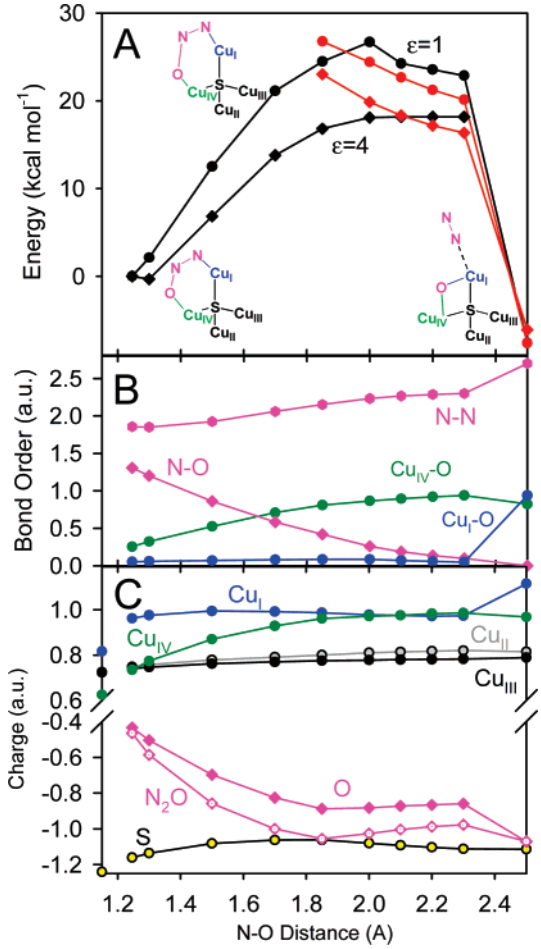

Figure 5. (A) Potential energy surfaces for the lowest-energy singlet (black lines) and triplet (red lines) states in a vacuum ($\epsilon = 1$) and in the dielectric medium (PCM($\epsilon = 4$)), (B) Mayer bond order profiles in the singlet state, and (C) NPA charges of the $[Cu_4S(im)_7N_2O]^{2+}$ complex in the singlet state along the reaction coordinate; BP86/PCM($\epsilon = 4$) calculations. The Cu and S atomic charges in the $[Cu_4S(im)_7]^{2+}$ complex are shown on the *Y*-axis for comparison.

sponding bond orders increase, Figure 5B) at the expense of the weaker N−O bond, and the Cu_I−N bond weakens only slightly. At the TS, there is complete transfer of an electron from Cu_{IV} to the N_2O ligand (with the oxygen atom carrying most of this charge, Figure 5C). This plays a very important role in the covalent and electrostatic stabilization of the TS (E_{int} = −73.2 kcal mol^{-1}, Figure 4). It also lowers the N−O bond cleavage barrier from 25 ($\epsilon = 1$) to 18 kcal mol^{-1} ($\epsilon = 4$) by electrostatic stabilization of the TS in the dielectric environment (Figure 5A). Since the charge of the N_2O ligand is higher in the TS than in the reactant state (Figures 4 and 5C), additional noncovalent interactions (such as hydrogen bonds between the oxygen atom of the N_2O ligand and the protons of the neighboring amino acids, see section 3.3) can further lower the activation energy. Thus, 18 kcal mol^{-1} is only an upper estimate for the activation barrier of the N−O bond cleavage.

When the N−O distance is elongated from 1.8 to 2.2 Å, the Cu_{IV}^{2+}−O^- bond continues to strengthen, and the N−O bond is almost completely broken (Figure 5B). At the final step of the reaction coordinate (when the N−O distances are longer than 2.2 Å), the Cu_I atom transfers an electron to the oxygen (Figure 5C), the $2Cu^{II}/2Cu^{I}$ species with an oxo bridge (O^{2-}) is formed (Figure 5B, blue line), and the Cu_I−N bond is broken. The Cu_I−O bond (Figure 5B) provides a substantial thermodynamic stabilization of the $[Cu_4S(im)_7O]^{2+}$ ($2Cu^{II}/2Cu^{I}$) species and drives the cleavage step to completion (Figure 5A).

In summary, the direct cleavage of the N−O bond in the $[Cu_4S(im)_7N_2O]^{2+}$ complex involves bringing the N_2O linear molecule to the bent, activated geometry of the transition state (Figure 4). The deformation energy required for N_2O activation is compensated by formation of the strong Cu_{IV}−O bond and stronger noncovalent interactions between the polar TS and the protein environment. Thus, there are two requirements for the N_2OR catalytic site: (1) the binding site for N_2O must contain two metal centers, M_a and M_b, which are able to bind to N_2O in a μ-1,3 bridging mode, so that the energy associated with the N−O bond cleavage can be compensated by the energy from the two metal−ligand bonds (M_a−N_2 and M_b−O, Figure 5B) in the TS, and (2) the metal centers have to be good electron donors in their reduced state, so that they can bind the weak π acceptor N_2O molecule with a high enough affinity to form the reactant complex and generate a polar TS with significant charge transfer to the N_2O ligand (Figure 5C).

3.3. Role of H-Bonding and Protonation in the Reaction Coordinate. The analysis of the reaction coordinate for the N−O bond cleavage (section 3.2) shows that charge transfer from the Cu_Z cluster to the N_2O ligand plays a very important role in lowering the activation barrier through the greater interaction energy of the Cu_Z and N_2O fragments in the TS relative to the reactant complex. In the TS, there is complete transfer of an electron from Cu_Z to the N_2O ligand (Figure 5C). The shift of electron density from Cu_Z to N_2O activates the oxygen atom of the latter for H-bonding and protonation. The available protein structural data suggest that the Lys464 residue[8] (Figure S2) near the Cu_I/Cu_{IV} edge of the Cu_Z cluster can participate in this stage. Since the negative charge of the oxygen atom is much higher in the TS than in the reactant complex, H-bonds between the oxygen atom of the N_2O ligand and the protons of the neighboring amino acid residues can be expected to lower $\Delta G^{\ddagger}$ of the N−O bond cleavage.

We have evaluated the influence of H-bonds of different strengths on the activation barrier for the N−O bond cleavage in $[Cu_4S(im)_7N_2O]^{2+}$ by constructing molecular models where one H-bond is formed between the N_2O ligand and a neighboring water molecule or where the H-bond is formed between N_2O and a formic acid molecule (HCOOH). The calculations indicate that $\Delta G^{\ddagger}$ is lowered by ∼5 kcal mol^{-1} if H_2O is the proton donor, and by ∼9 kcal mol^{-1} if HCOOH is the proton donor. Thus, the stronger acidity of the H-bond donor produces greater TS stabilization. In an extreme case, where the gas-phase proton H^+ assists in the N−O bond cleavage, the activation barrier for the N−O bond cleavage is eliminated.

In summary, the barrier for the direct cleavage of the N−O bond can be lowered from $\Delta G^{\ddagger}$ = 18 kcal mol^{-1} (PCM(ϵ = 4)) to $\Delta G^{\ddagger}$ = 9−13 kcal mol^{-1} by noncovalent H-bond interactions. Moreover, if the proton transfer is coupled with the direct N−O cleavage step, the activation barrier can be reduced further to zero. Thus, at low pH values (4−8), the rate-limiting step in the catalytic cycle of N_2OR is likely to be electron transfer (ET) to the Cu_Z cluster from the reductant via the ET site (Cu_A in Cu-only N_2ORs or *c*-type cytochrome in copper−iron N_2ORs) rather than the N−O bond cleavage.

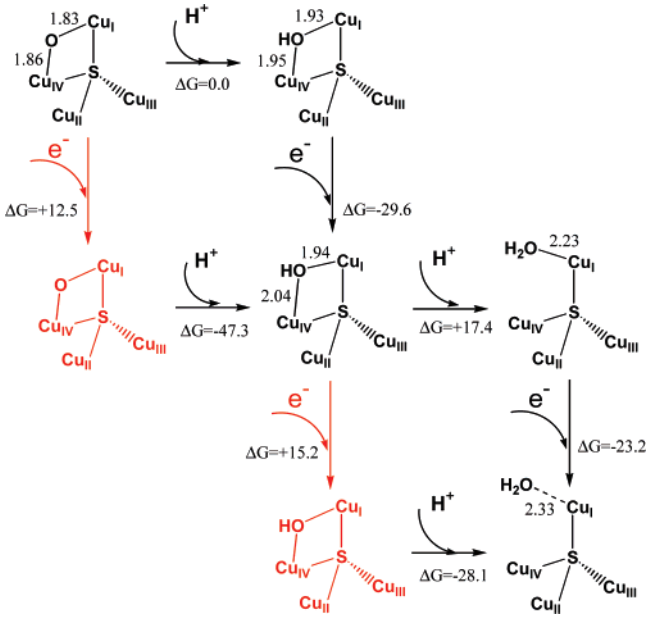

Figure 6. Redox forms of the Cu_Z cluster which are relevant for the catalytic cycle in N_2OR. The imidazole ligands of the Cu_Z cluster have been removed from the structures for simplicity. The interactomic distances are given in Å. Free energies (kcal mol^{-1}) of the steps are calculated at 298 K, taking into account that Cu_A is the electron donor and the bulk water is the source of protons (see Computational Details). The energetically unfavorable species are shown in red and the corresponding reaction energies do not include ZPE and thermal corrections.

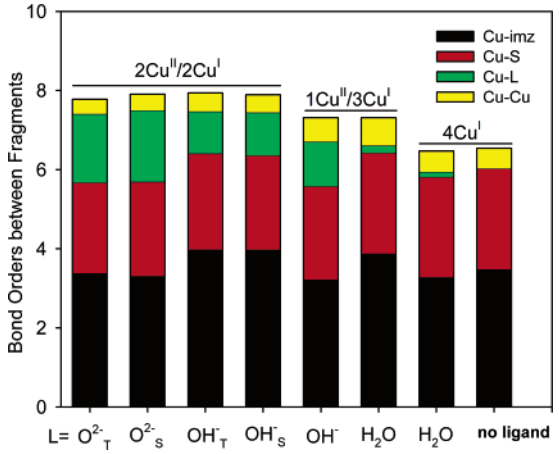

Figure 7. Metal−ligand (Cu−S, red; Cu−imz, black; Cu−L, green) and metal−metal (Cu−Cu, yellow) bond orders in the $[Cu_4S(im)_7L]^{q+}$ species.

3.4. Thermodynamic Cycle. After the first step of the reaction (the N−O bond cleavage), the Cu_Z site is in the $2Cu^{II}/2Cu^{I}$ redox state and has to undergo two one-electron reductions and two protonation steps (Figure 6) in order to return to the catalytically active redox state $4Cu^{I}$. The free energies of these steps were calculated assuming that Cu_A is an electron donor for the Cu_Z reduction steps, its absolute redox potential is 4.76 V, and the proton solvation energy is 262.23 kcal mol^{-1} (see Computational Details).

The geometric and electronic structures of the possible intermediates were evaluated using Mayer bond order calculations (Figure 7; Tables 1 and S6) and electron population analyses (Figures 8 and 9; Tables S4, S5, and S7).

The direct cleavage product, $[Cu_4S(im)_7O]^{2+}$, has two Cu^{II} atoms (Cu_I and Cu_{IV}) with one unpaired electron each (Tables S4 and S5). The O^{2-} ligand forms a bridge at the Cu_I/Cu_{IV} edge,

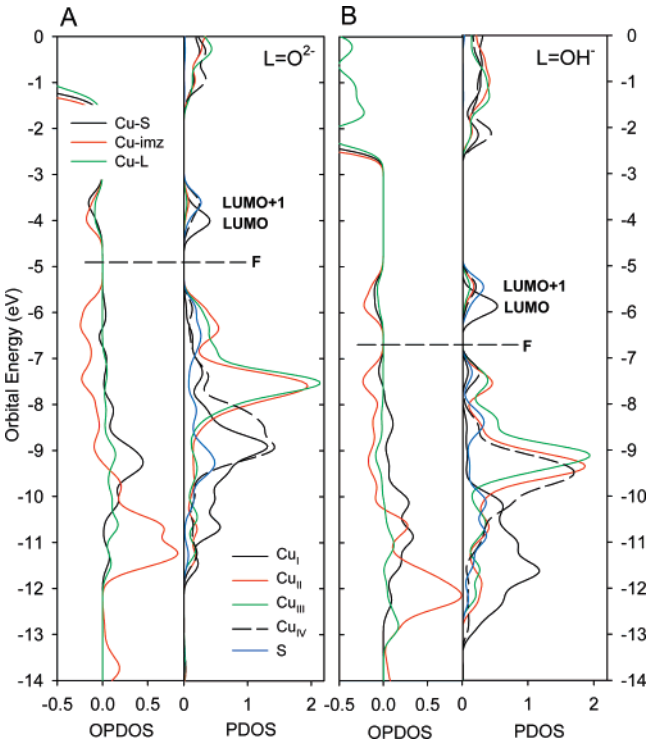

Figure 8. β-Spin overlap population-based density of states (OPDOS) and contributions of the Cu and S atoms of the Cu_Z cluster to the density of states (PDOS) of the $[Cu_4S(im)_7L]^{q+}$ species (A, L = O^{2-}; B, L = OH^-) in a $2Cu^{II}/2Cu^{I}$ redox state (spin triplet).

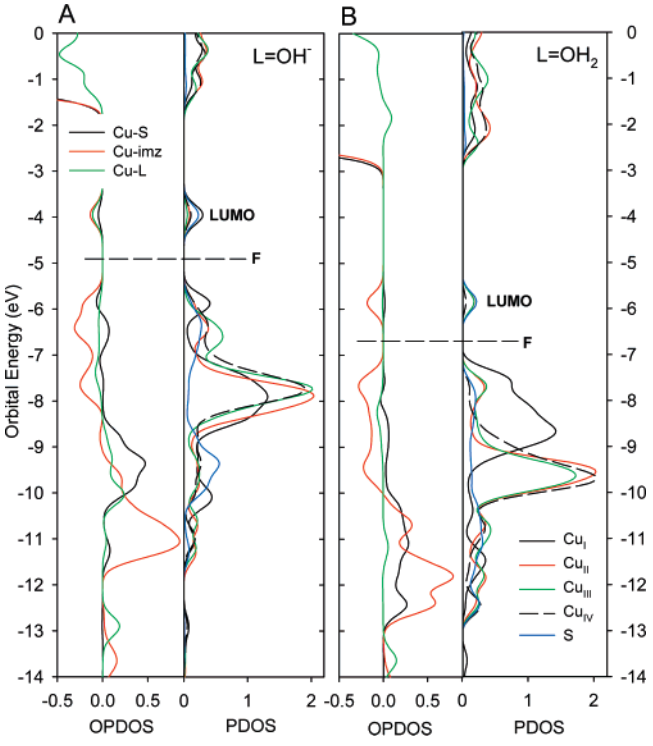

Figure 9. β-Spin overlap population-based density of states (OPDOS) and contributions of the Cu and S atoms of the Cu_Z cluster to the density of states (PDOS) of the $[Cu_4S(im)_7L]^{q+}$ species (A, L = OH^-; B, L = OH_2) in a $1Cu^{II}/3Cu^{I}$ redox state.

and the corresponding Cu−O bond distances are 1.83−1.86 Å (Figure 6). The two unpaired electrons of the Cu_Z cluster in the $2Cu^{II}/2Cu^{I}$ redox state can couple ferromagnetically or antiferromagnetically, producing spin-triplet and spin-singlet states.

Table 1. Cu−S Bond Lengths and the $Cu_4S(im)_7$-L Bond Orders of the $[Cu_4S(im)_7L]^{q+}$ Species

	bond orders, au					Cu–S distances, Å			
species[a]	Cu_Z–L[b]	α[b]	β[b]	Cu_I–L	Cu_{IV}–L	Cu_I–S	Cu_{II}–S	Cu_{III}–S	Cu_{IV}–S
$Cu_4S(im)_7(O)^{2+}$ T	1.90	0.57	1.33	0.98	0.75	2.676	2.199	2.232	2.335
$Cu_4S(im)_7(O)^{2+}$ S	1.92	0.96	0.96	0.88	0.87	2.460	2.225	2.250	2.357
$Cu_4S(im)_7(O)^{+}$	1.89	0.76	1.13	0.91	0.83	2.485	2.188	2.245	3.515
$Cu_4S(im)_7(OH)^{3+}$ T	1.07	0.43	0.64	0.58	0.47	2.598	2.199	2.235	2.413
$Cu_4S(im)_7(OH)^{3+}$ S	1.11	0.51	0.60	0.63	0.46	2.555	2.206	2.231	2.413
$Cu_4S(im)_7(OH)^{2+}$	0.97	0.39	0.58	0.55	0.38	2.444	2.261	2.234	2.292
$Cu_4S(im)_7(OH)^{+}$	0.89	0.45	0.45	0.53	0.35	3.203	2.127	2.256	2.386
$Cu_4S(im)_7(H_2O)^{3+}$	0.21	0.10	0.11	0.18	0.03	2.402	2.345	2.212	2.159
$Cu_4S(im)_7(H_2O)^{2+}$	0.15	0.07	0.07	0.13	0.01	2.320	2.339	2.263	2.148
$Cu_4S(im)_7^{2+}$						2.270	2.328	2.269	2.150

[a] S, singlet state; T, spin triplet state. [b] Mayer bond order between the $[Cu_4S(im)_7]$ cluster and the Cu_I/Cu_{IV} edge ligand L and its α- and β-spin orbital components, respectively.

The BS singlet and triplet states of the $[Cu_4S(im)_7O]^{2+}$ intermediate are very close in energy ($\Delta E = 0.6$ kcal mol^{-1} with the triplet being at lower energy in the gas phase, and $\Delta E = 1.4$ kcal mol^{-1} with the singlet being at lower energy in the PCM($\epsilon = 4$) calculations), and both states have electron spin density localized on Cu_I, Cu_{IV}, and S. According to the bond order analysis, in the triplet state, the bridging oxygen atom forms two covalent bonds with the Cu_I and Cu_{IV} atoms through interactions involving Cu 4s, 4p, and 3d orbitals (the α- and β-spin MO bond order contributions for the Cu_Z−O interaction are 0.57 and 1.33 (Table 1), respectively). The Cu_I−O and Cu_{IV}−O bond orders are 0.98 and 0.75, respectively (Table 1). Thus, the oxygen has a stronger covalent bond to Cu_I than to Cu_{IV}. The atomic spin densities (SDs) on Cu_I, Cu_{IV}, and S are 0.46, 0.28, and 0.37, respectively (Table S4). The compositions of the β-spin LUMO and LUMO + 1 (Table S7) reflect the above spin densities. As can be seen from the overlap-population density-of-state (OPDOS) plot (Figure 8A), both of these MOs have negative metal−ligand overlap populations, and, thus, the LUMO and LUMO + 1 are antibonding with respect to Cu−ligand (S, imz, O) orbital interactions.

In the singlet state, the Cu_I−O and Cu_{IV}−O bond orders are 0.88 and 0.87, respectively (Table 1), indicating equal covalencies of these interactions. The unpaired electron on Cu_I (0.44) is anti-ferromagnetically coupled with the unpaired electrons on Cu_{IV} (−0.29) and S (−0.19). The Cu_{II} and Cu_{III} SD is less than 0.01 for the singlet, and 0.05 and 0.03, respectively, for the triplet state (Table S4).

The calculated energies of the protonation and reduction of the $[Cu_4S(im)_7O]^{2+}$ species indicate that the protonation is an energetically favorable step, with $\Delta G = 0.0$ kcal mol^{-1} (Figure 6). The addition of the proton transforms the O^{2-} bridge to an OH^- bridge at the Cu_I/Cu_{IV} edge. Upon protonation, the Cu_I−O and Cu_{IV}−O bond distances increase by ∼0.1 Å to 1.93−1.95 Å. The BS singlet and triplet states of the $[Cu_4S(im)_7OH]^{3+}$ intermediate are again very close in energy ($\Delta E = 1.4$ and 0.2 kcal mol^{-1} in the gas-phase and the $\epsilon = 4$ dielectric medium, respectively). However, the unpaired electrons in $[Cu_4S(im)_7OH]^{3+}$ are now much more delocalized than in $[Cu_4S(im)_7O]^{2+}$. In the lowest-energy (triplet) state, the NPA-derived SDs (Table S4) are 0.56 (Cu_I), 0.18 (Cu_{II}), 0.14 (Cu_{III}), 0.21 (Cu_{IV}), and 0.51 (S). The β-spin LUMO and LUMO + 1 of this species are antibonding with respect to the metal−ligand (S, imz, O) interactions, and the corresponding overlap populations are negative (Figure 8B). In the singlet state, the unpaired electron on Cu_I (SD of 0.67) is anti-ferromagnetically coupled to the unpaired electron on the remaining atoms of the Cu_Z cluster, with each atom carrying a SD of 0.18−0.22 (Table S4).

The calculated energies of the protonation and reduction of the $[Cu_4S(im)_7OH]^{3+}$ species indicate that electron transfer from the reduced Cu_A center to the Cu_Z site is now energetically favorable ($\Delta G = -29.6$ kcal mol^{-1}). The $[Cu_4S(im)_7OH]^{2+}$ species formed has one unpaired electron, which is mostly localized on Cu_I and S (SD of 0.30 on each, Table S4), with small contributions from the other Cu atoms (Cu_{II}, 0.07; Cu_{III}, 0.05; Cu_{IV}, 0.10). The electronic polarizability of the Cu_Z cluster is quite high, and the above spin distribution can be influenced by the electrostatics of the protein. The OH^- ligand remains at the Cu_I/Cu_{IV} edge as a bridging ligand. However, the bond order (Table 1) between the Cu_I atom and the OH^- ligand, BO_{Cu_I-OH}, is 0.55, relative to the $BO_{Cu_{IV}-OH}$ of 0.38, indicating that OH^- is more strongly bound to Cu_I than to Cu_{IV}. The α- and β-spin components of the bond orders for orbital interactions between the Cu_Z cluster and the OH^- ligand (Table 1) indicate that the Cu_Z−OH^- covalent bonding comes from orbital interactions of the OH^- ligand with Cu 4s,4p orbitals and, to a lesser degree, from the unoccupied β-spin Cu 3d levels. The β-spin LUMO of the complex (Table S7; Figure 9A) is a weakly antibonding orbital with respect to the Cu−ligand interactions. Since the antibonding molecular orbital of the $2Cu^{II}/2Cu^{I}$ species is now occupied in $[Cu_4S(im)_7OH]^{2+}$, there is an overall decrease in covalent bonding relative to that of $2Cu^{II}/2Cu^{I}$ species (the sum of the Cu_Z cluster bond orders decreases, Figure 7).

The protonation of the $[Cu_4S(im)_7OH]^{2+}$ species is a favorable step at low and neutral pH (Figure 6). After protonation, the species is converted to $[Cu_4S(im)_7H_2O]^{3+}$, which is likely the species that has been spectroscopically characterized at low and neutral pH.[17−19] The spectroscopic study of *P. nautica* N_2OR indicates that the equilibrium between the $[Cu_4S(im)_7OH]^{2+}$ and $[Cu_4S(im)_7H_2O]^{3+}$ species has pK_a of ∼8.5.[17] In the $[Cu_4S(im)_7H_2O]^{3+}$ species, the water ligand is bound to only one Cu atom (Cu_I), and, as a result of the high coordination number (CN = 4) of Cu_I relative to the other Cu atoms (CN = 2−3), this copper atom carries a higher charge and SD than the other copper atoms in the Cu_Z cluster (Table S4). The bond order analysis (Table 1; Figure 7, $1Cu^{II}/3Cu^{I}$, green) indicates that the H_2O is weakly bound ($E_o = -13$ kcal mol^{-1}, Table S1) relative to the OH^- ligand and the Cu_Z-OH_2 covalent bonding comes from orbital interactions of the water ligand with Cu 4s,-4p orbitals, with almost no contribution from the β-spin LUMO. The unpaired electron in $[Cu_4S(im)_7H_2O]^{3+}$ is delocalized on the Cu_Z cluster atoms (Table S4), and this delocalization

activates the superexchange pathways for electron transfer from the reduced Cu_A site through the Cu_{II} and S atoms with a driving force of -23.2 kcal mol^{-1}. After electron transfer from Cu_A, the Cu_Z cluster returns to the catalytically active redox form, $4Cu^I$.

Comparison of the fully reduced $[Cu_4S(im)_7H_2O]^{2+}$ complex and the $[Cu_4S(im)_7]^{2+}$ species (where the Cu_I/Cu_{IV} edge ligand is absent) shows little difference (Tables 1 and S4; Figure 7). This is a reflection of the very weak interaction between the water ligand and the Cu_I atom in the $4Cu^I$ redox form (the Cu_I-O distance is 2.33 Å, $BO(Cu_Z-OH_2) = 0.15$, and $E_o(Cu_Z-OH_2) = -7$ kcal mol^{-1} (Table S1) in the gas phase). As a result, the H_2O ligand can be displaced by the N_2O molecule with a small activation barrier (less than 7 kcal mol^{-1}, the dissociation energy of the weak Cu_I-OH_2 complex).

3.5. Contributions to Reactivity. 3.5.1. Role of the $4Cu^I$ Redox State of Cu_Z in N_2O Binding. It has been established that the Cu_Z site in the resting form of N_2OR is in the $1Cu^{II}/3Cu^I$ redox state.[17,19] In order for the enzyme to function, Cu_Z must bind the N_2O molecule. We have evaluated the N_2O binding to the Cu_Z cluster in the $1Cu^{II}/3Cu^I$ state. This redox state is able to bind N_2O in an end-on coordination mode (through the terminal N atom), and the corresponding gas-phase binding energy (Table S1) is -6.7 (BP86) and -4.6 kcal mol^{-1} (B3LYP). However, if we consider the competitive binding of the N_2O molecule versus the H_2O ligand to the Cu_Z cluster, the free energy of the reaction

$$[Cu_4S(im)_7H_2O]^{3+} + N_2O \rightarrow [Cu_4S(im)_7N_2O]^{3+} + H_2O \quad (5)$$

in the gas phase is positive: $+6.3$ (BP86) and $+8.6$ kcal mol^{-1} (B3LYP). According to the PCM calculations (Table S1), ΔG_r in the dielectric continuum ($\epsilon = 4$) is also positive: $+5.5$ (BP86) and $+7.5$ kcal mol^{-1} (B3LYP). Thus, the equilibrium constant corresponding to eq 5 is very small ($10^{-4}-10^{-6}$) and eliminates the N_2OR catalytic function. The analysis of the charge distributions in the $[Cu_4S(im)_7H_2O]^{3+}$ and $[Cu_4S(im)_7N_2O]^{3+}$ complexes indicates that the net charge transfer from the ligand to the Cu_Z cluster is greater for the H_2O complex ($q_{NPA}(H_2O) = 0.04$ au) than for the N_2O complex ($q_{NPA}(N_2O) = -0.01$ au). This is consistent with the fact that H_2O is a stronger σ donor ligand than N_2O, and the interaction with a stronger ligand explains the greater stability of the $[Cu_4S(im)_7H_2O]^{3+}$ complex relative to $[Cu_4S(im)_7N_2O]^{3+}$.

Alternatively, the $4Cu^I$ redox state of the Cu_Z cluster binds both N_2O and H_2O with low affinity. The $4Cu^I$ redox state lessens the binding of σ donor ligands but enhances the binding of π acceptor ligands. As a result, the energy of the reaction

$$[Cu_4S(im)_7H_2O]^{2+} + N_2O \rightarrow [Cu_4S(im)_7N_2O]^{2+} + H_2O \quad (6)$$

is close to zero: -0.1 (BP86, PCM($\epsilon = 4$)) and $+3.5$ kcal mol^{-1} (B3LYP, PCM($\epsilon = 4$)). This allows the Cu_Z site of the N_2OR to bind N_2O for the reductive cleavage of the N−O bond.[88]

(88) The one experimental estimate[11,12] of K_m is 2.5 μM, which corresponds to a N_2O binding free energy (eq 6) of $\Delta G = -7.5$ kcal mol^{-1}. Note that there are allosteric effects[11] which can complicate this estimate. To allow a direct comparison, our calculated values, -0.1 (BP86) and $+3.5$ kcal mol^{-1} (B3LYP), should be corrected by ~ 7 kcal mol^{-1} to account for solvation of the displaced water. Any additional H-bonding at the site (as discusssed in section 3.2) would also affect the N_2O binding energy.

3.5.2. Role of the μ_4-Sulfide-Bridged Tetranuclear Copper Cluster. As has been determined in section 3.2, the participation of the Cu_{II} and Cu_{III} atoms of the Cu_Z ($4Cu^I$) site in the N−O bond cleavage of the N_2O molecule is very limited. Their atomic charges hardly change during the N−O bond cleavage (Figure 5C). To establish the role of the μ_4-S, Cu_{II}, and Cu_{III} atoms of the Cu_Z cluster, we evaluated the reaction coordinate of N−O bond cleavage with three perturbed Cu_Z models: model A, the μ_4-bridging S atom was replaced by the μ_4-bridging O atom; model B, the Cu_{II} and Cu_{III} atoms were substituted with Zn^{II} ions; and model C, the Cu_{II} and Cu_{III} ions, together with the imidazole ligands which are coordinated to Cu_{II} and Cu_{III}, were removed.

The $[Cu_4O(im)_7]^{2+}$ species (model A) shows no N_2O binding. This can be attributed to the facts that oxygen is more electronegative than sulfur and, in the $[Cu_4O(im)_7]^{2+}$ cluster, Cu_I and Cu_{IV} carry more positive charge than in the $[Cu_4S(im)_7]^{2+}$ cluster (the Cu−S bond is more covalent than the Cu−O bond in these clusters). The higher atomic charges of Cu_I and Cu_{IV} make these atoms weaker back-donors, hampering N_2O binding.

The reaction coordinate of the N−O bond cleavage in the remaining two models shows steps and changes similar to those observed for $[Cu_4S(im)_7N_2O]^{2+}$. The computed activation barriers for the N−O bond cleavage (Table S8) are 27 (model B) and 18 kcal mol^{-1} (model C), and the N−O bond distance at the TS is 1.7−1.9 Å. The protein strain energies, E_{strain} (section 3.4.4), of models A and C (8 and 36 kcal mol^{-1}, respectively, Table S8) do not exceed those of the $[Cu_4S(im)_7]$ species. However, E_{strain} for model B is greater than 80 kcal mol^{-1} (Table S8), indicating that this high-charge ($q = 4+$) cluster cannot be supported by the protein environment around the cluster.

The $[Cu_2S(im)_3(N_2O)]^{0+}$ species shows μ-1,3-N_2O binding at the Cu_I/Cu_{IV} edge similar to that displayed by the $[Cu_4S(im)_7(\mu\text{-}1,3\text{-}N_2O)]^{2+}$ complex (Figure S3A). In the absence of the N_2O ligand, $[Cu_2S(im)_3]^{0+}$ forms a new structure where one of the three imidazole ligands is H-bonded to the S^{2-} ion (Figure S3B). The N_2O binding to this cluster is energetically unfavorable (Table S8). The evaluation of the properties of the $[Cu_2S(im)_3]^{0+}$ species demonstrates that, unlike the $Fe^{II/III}_xS_y$ clusters, it has a very high proton affinity (the gas-phase value is 278 kcal mol^{-1}). Thus, under normal conditions in aqueous solution, the $[Cu_2S(im)_3]^{0+}$ complex would be protonated at the μ_2-S^{2-} atom and converted to the $[Cu_2SH(im)_3]^{+}$ species (Figure S3C). The latter binds the N_2O molecule ($\Delta E_f = -6.4$ (BP86) and -3.0 kcal mol^{-1} (B3LYP), Table S8). However, $[Cu_2SH(im)_3N_2O]^{+}$ has a much higher N−O cleavage barrier ($\Delta G^{\ddagger} = 37$ kcal mol^{-1}) than the $[Cu_4S(im)_7N_2O]^{2+}$ complex and a smaller driving force for the reaction ($\Delta G = -17.6$ kcal mol^{-1}, compared to -28.8 kcal mol^{-1} for the $[Cu_4S(im)_7N_2O]^{2+}$ complex), which make the Cu_2SH cluster a less efficient catalyst than the tetranuclear Cu_Z cluster. The reason for the higher activation energy is greatly reduced charge transfer from the $Cu_2SH(im)_3$ fragment to the N_2O ligand in the TS (Figure 10).

3.5.3. Protein Contribution. The Cu_Z cluster provides a binding site for the N_2O molecule at the Cu_I/Cu_{IV} edge of the cluster. To maintain this binding site, the protein can impose structural constraints through the covalent links with backbone and noncovalent interactions. It has been suggested that a complex network of hydrogen bonds determines the orientation

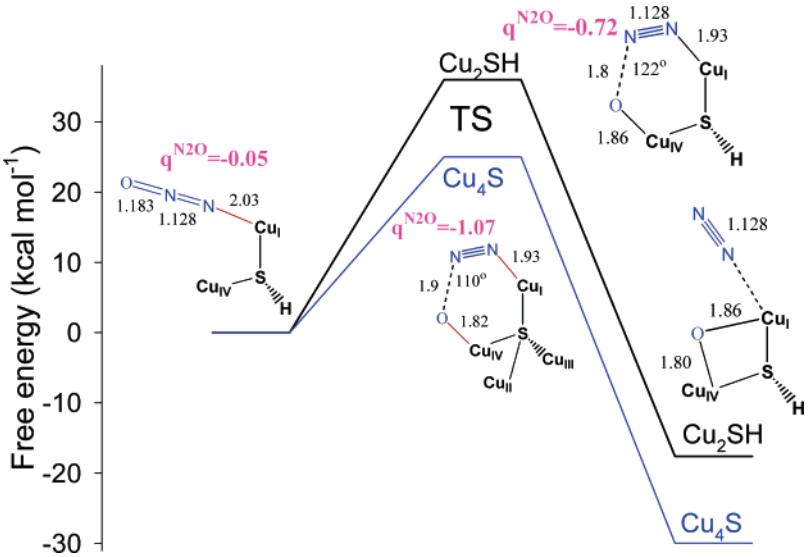

Figure 10. Reaction coordinate for N−O bond cleavage by the binuclear $[Cu_2SH(im)_3]^+$ cluster. For comparison, $\Delta G^{\ddagger}$ and ΔG_r for the $[Cu_4S(im)_7]^{2+}$ are shown in blue.

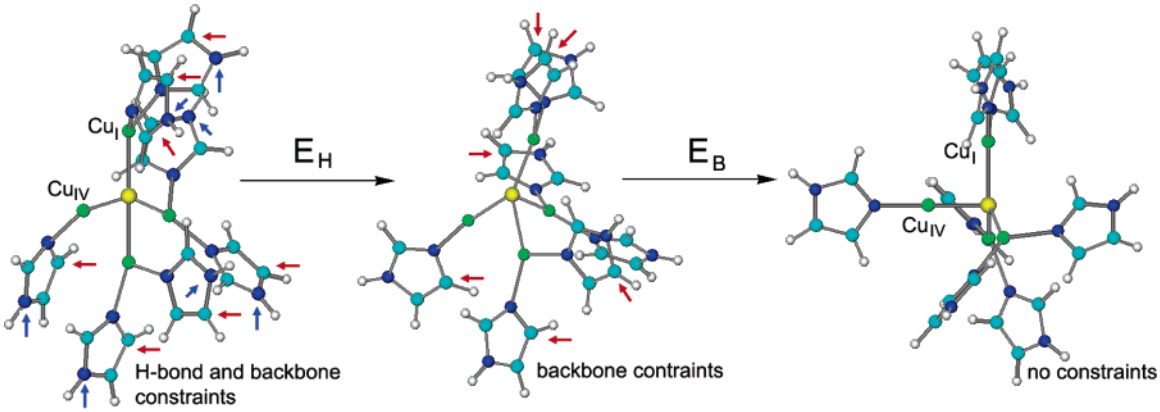

Figure 11. Rearrangement of the $[Cu_4S(im)_7]^{2+/3+}$ complexes upon removal of the protein-imposed constraints. The noncovalent (H-bond) and covalent (backbone) constraints are indicated by blue and red arrows, respectively.

of the imidazole side chains.[8] Our calculations are consistent with this suggestion and indicate that, without the H-bond support, the imidazole rings change their orientations and the tetranuclear copper cluster moves toward a distorted tetrahedral (trigonal pyramid) geometry of the Cu_4S cluster (Figure 11, left). If all constraints (backbone and noncovalent) are removed, the Cu_4S cluster rearranges (Figure 11, far right), adopting a trigonal pyramid geometry with the Cu_I, Cu_{II}, Cu_{III}, and S atoms at its base.[89] The Cu_Z cluster in this geometry has lost the Cu_I/Cu_{IV}-binding site and, with it, the ability to bind the N_2O molecule.

The calculated strain energies (Table 2, $E_{strain} = E_H + E_B$, where E_H and E_B are the strain energies related to noncovalent H-bond interactions and covalent protein backbone constraints, respectively) from the B3LYP and BP86 calculations are very similar and indicate that the protein provides a support for maintaining the structure of the Cu_Z cluster with the Cu_I/Cu_{IV}-binding site. The H-bond network imposes a greater strain on the cluster structure than the covalent connections to the protein backbone through the C_α atoms. The protein support required to maintain the Cu_Z cluster site is greater for the cluster with higher total charge (Table 2). For the species in the reaction cycle, E_{strain} shows a similar trend: 33.8 (for $[Cu_4S(im)_7O]^{2+}$), 28.4 (for $[Cu_4S(im)_7OH]^{2+}$), and 33.2 kcal mol^{-1} (for $[Cu_4S(im)_7OH_2]^{2+}$), versus 35.7 (for $[Cu_4S(im)_7OH]^{3+}$) and 43.3 kcal mol^{-1} (for $[Cu_4S(im)_7OH_2]^{3+}$). Since the protein strain energies are higher for the higher charged species, the protein strain influences the redox potentials and protonation free energies of the reaction intermediates by as much as 0.4 V and 15 kcal mol^{-1}, respectively.

Table 2. Strain Energies of the Cu_Z Cluster (E_{strain}) through Covalent Bonds (E_B) and Noncovalent Interactions (E_H) at the B3LYP and BP86 Level of Theory[a]

species	E_{strain}, kcal mol^{-1}	E_H, kcal mol^{-1}	E_B, kcal mol^{-1}
$[Cu_4S(im)_7]^{2+}$	32.3 (29.8)	20.0 (20.3)	12.3 (9.5)
$[Cu_4S(im)_7]^{3+}$	41.5 (38.7)	25.0 (24.2)	16.5 (14.5)

[a] The BP86 results are shown in parentheses for comparison.

The strain energies obtained are higher than those reported for blue copper sites in metalloproteins (7.2−19.6 kcal mol^{-1}).[90−92] However, taking into account the size of the Cu_Z cluster and the facts that the strain is imposed through seven

(89) The structure of the Cu_4S cluster with eight imidazole ligands is tetrahedral. Removal of one imidazole ligand from $[Cu_4S(im)_8]^{q+}$ and the consequent re-optimization leads to a trigonal pyramidal structure, which is a true energy minimum with all real vibrational frequencies. This structural change comes from the preference of the fully reduced Cu^I ion with one Im ligand for a linear ligand environment (the S−Cu−N(Im) angle is 180°). Optimizations of the $[Cu_4S(im)_7]^{q+}$ species using other starting points also give the trigonal pyramidal structure of the Cu_4S cluster.

H-bonds and seven covalent bonds and each N(im)···H−O hydrogen bond is ∼4−5 kcal mol^{-1}, the noncovalent and backbone contributions to E_{strain} do not exceed a reasonable limit for a metal cluster site in the protein.

4. Discussion

The Cu_Z site of N_2OR binds and activates the N_2O molecule for reductive cleavage. The role of the fully reduced μ_4-sulfide-bridged tetranuclear copper cluster has been defined from evaluation of several molecular models ($[Cu_4S(im)_7]^{2+}$, $[Cu_4S(im)_7]^{3+}$, $[Cu_4O(im)_7]^{2+}$, $[Cu_2S(im)_3]^{0+}$, and $[Cu_2SH(im)_3]^{+}$). In its $4Cu^I$ state, the Cu_Z cluster turns off binding of stronger donor ligands (H_2O) while enabling the formation of a bent μ-1,3-N_2O−Cu_Z complex through enhanced $Cu_Z \rightarrow N_2O$ back-donation. The Cu_I and Cu_{IV} atoms at the ligand-binding site of the cluster are critical to the enzymatic function; these atoms are directly involved in N_2O binding and reduction. The other atoms of the Cu_Z cluster are required for extensive back-bonding. The low reaction barrier of the direct cleavage of the N−O bond (Figure 5A) is achieved by N_2O activation in the reactant complex and TS stabilization by the charge transfer, which leads to a strong Cu_{IV}−O bond. If the N−O bond cleavage is coupled to protonation, the process can become barrierless. The H-bond network and the backbone of the protein near the catalytic site provide structural support for the distorted tetrahedral geometry of the Cu_Z cluster, and noncovalent interactions help to lower the activation energy of the N−O bond cleavage through the preferential stabilization of the polar TS relative to the reactant complex with less $Cu_Z \rightarrow N_2O$ charge transfer. After N−O cleavage, the catalytic cycle consists of a sequence of alternating protonation/one-electron reduction steps which returns the Cu_Z cluster to the fully reduced form (Figure 6).

Since nitrous oxide is both a weak σ donor and a weak π acceptor ligand,[50] its binding to metal sites and activation for the N−O bond cleavage are difficult to achieve. The Cu_Z site accomplishes this goal through extensive charge transfer from the metal cluster to the N_2O ligand. To maximize this charge transfer, $Cu_Z \rightarrow N_2O$ back-donation has to be large and $N_2O \rightarrow Cu_Z$ donation small. The LCFO-MO analysis (Scheme 1; Table S3) and the natural population analysis (NPA)[73] can be used to evaluate donation and back-donation in the Cu_Z−N_2O complexes with μ-1,3-bent and linear end-on coordinations of N_2O, and in the well-defined $[Ru^{II}(NH_3)_5(N_2O)]^{2+}$ complex as a reference, for which there have been discussions on the extent of σ $N_2O \rightarrow$ Ru donation and π Ru $\rightarrow N_2O$ back-donation.[48,50] For the $[Cu_4S(im)_7(\mu\text{-}1,3\text{-}N_2O)]^{2+}$ complex, NPA indicates a larger decrease in Cu 3d orbital populations with only a small increase in Cu 4s,4p orbital populations, compared to the Cu atoms in the Cu_Z cluster without the N_2O ligand. These changes in orbital populations correspond to very substantial π $Cu_Z \rightarrow N_2O$ back-donation but weak σ $N_2O \rightarrow Cu_Z$ donation and produce a net large charge transfer (0.49 e$^-$, Figure 4) to the bent N_2O ligand.

In the $[Ru^{II}(NH_3)_5(N_2O)]^{2+}$ complex, the π back-donation is much less (∼0.2 vs 0.6 e$^-$ in $[Cu_4S(im)_7(\mu\text{-}1,3\text{-}N_2O)]^{2+}$) and is equal in magnitude to σ $N_2O \rightarrow$ Ru donation. As a result, the N_2O ligand in the Ru complex has a very small charge (−0.03 au, Table S3). The $[Cu_4S(im)_7N_2O]^{2+}$ complex with the linear end-on coordination of N_2O displays σ $N_2O \rightarrow Cu_Z$ donation and π $Cu_Z \rightarrow N_2O$ back-donation that are similar in magnitude to those in the Ru complex. However, while in $[Ru^{II}(NH_3)_5(N_2O)]^{2+}$ the $N_2O \rightarrow$ M donation involves the orbital interaction between the HOMO − 2(N_2O) donor orbital and the LUMO d_{z^2} acceptor orbital of the $Ru(NH_3)_5^{2+}$ fragment, for the Cu^+ ion the d_{z^2} orbital is filled and cannot contribute to net Cu−N_2O ligand donor bonding. As a result, the $N_2O \rightarrow Cu^I$ donation is only due to weaker interactions with the Cu 4s,4p acceptor orbitals. The energy of the π* LUMO of the linear N_2O is too high to form a strong π $Cu_Z \rightarrow N_2O$ back-bond (Figure 12, left). Thus, in a linear N-end-on Cu_Z−N_2O complex, nitrous oxide is not activated (the ligand deformation energy and net charge transfer to N_2O are close to zero (Figure 4), and the charge on the oxygen atom is less negative than in the free molecule). In contrast, in the μ-1,3-N_2O−Cu_Z complex, the π* LUMO of the bent N_2O ligand (Figure 12, right) has a much lower energy than a linear N_2O molecule and forms a strong π $Cu_Z \rightarrow N_2O$ back-bond with the occupied d orbitals of the Cu_Z cluster. This interaction activates nitrous oxide for N−O bond cleavage (the N−O bond is elongated and the N_2O deformation energy, 18.6 kcal mol^{-1}, reduces the activation barrier for N−O bond cleavage, Figure 4).

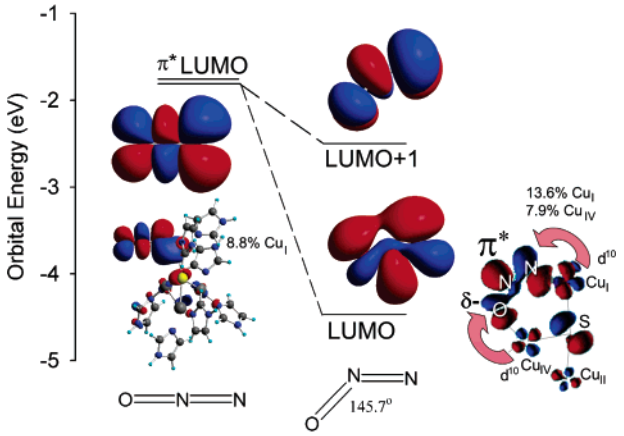

Figure 12. LUMOs of the linear and bent N_2O molecules and the LUMOs of the corresponding linear and μ-1,3-bridged Cu_Z−N_2O complexes (BP86/TZVP calculations).

The π $Cu_Z \rightarrow N_2O$ back-donation is further influenced by the polarity of the medium. Higher medium polarity increases $Cu_Z \rightarrow N_2O$ back-donation but does not affect $N_2O \rightarrow Cu_Z$ donation. As a result, the charge on the N_2O ligand in the $[Cu_4S(im)_7(\mu\text{-}1,3\text{-}N_2O)]^{2+}$ complex changes from −0.4 (gas-phase) to −0.5 au (PCM($\epsilon = 4$)). This effect is important in stabilization of the complex with a μ-1,3-bridging mode in a dielectric medium of the protein, relative to the less-polar complex with the linear N-end-on coordination of N_2O (section 3.2, Figure 4). This also helps to activate nitrous oxide for proton-assisted N−O bond cleavage. Due to its more negative charge (−0.43 au), the oxygen atom of the N_2O ligand is activated for electrophilic attack by a proton (section 3.3).

In summary, charge transfer from the fully reduced Cu_Z cluster is maximized by the d^{10} configuration of the copper atoms, which makes the cluster a very good donor with $Cu_Z \rightarrow N_2O$ back-bonding through high-energy, fully filled Cu 3d levels

(90) De Rienzo, F.; Gabdoulline, R. R.; Wade, R. C.; Sola, M.; Menziani, M. C. *CMLS, Cell. Mol. Life Sci.* **2004**, *61*, 1123.
(91) Ryde, U.; Olsson, M. H.; Pierloot, K.; Borin, A. C. *Theor. Chem. Acc.* **2001**, *105*, 452.
(92) Comba, P.; Lledos, A.; Maseras, F.; Remenyi, R. *Inorg. Chim. Acta* **2001**, *324*, 21.

and no $N_2O \rightarrow$ Cu $3d^{10}$ donation. The $Cu_Z \rightarrow N_2O$ back-donation is enhanced by low-energy π^* LUMO of the bent N_2O ligand (Figure 12). The $Cu_Z \rightarrow N_2O$ charge transfer and strong interaction of the μ-1,3-N_2O ligand with two redox-active Cu_I and Cu_{IV} atoms provide a low activation energy pathway for the N−O cleavage process, which involves two electrons. This mechanism may also be important for other systems, since M_a−N−N−O−M_b bridged species have been proposed as possible intermediates in the reductive cleavage of the N−O bond in Ru^{II} and Co^{I} complexes.[33,43,47] Since the N_2O binding and activation in N_2OR are achieved by the Cu_I and Cu_{IV} atoms of a preorganized Cu_Z cluster, this makes it a more effective catalytic center than the previously investigated molecular systems.

Acknowledgment. This research is supported by NIH grant DK-31450 (E.I.S.). S.I.G. is grateful to NSERC (Ottawa) for a postdoctoral fellowship.

Supporting Information Available: Complete ref 52, atom coordinates of the optimized structures of the Cu_Z complexes, and a summary of calculated electronic parameters. This material is available free of charge via the Internet at http://pubs.acs.org.

JA055856O